Model-Based Estimation of Flow Characteristics Using an Ionic Polymer–Metal Composite Beam

Xuefei Chen, Guoming Zhu, Xiaojian Yang, David L. S. Hung, and Xiaobo Tan, *Senior Member, IEEE*

***Abstract*—An ionic polymer–metal composite (IPMC) beam is capable of producing an electric signal closely correlated with its mechanical movement, due to the redistribution of mobile ions inside the IPMC material. Motivated by the potential application of this intrinsic sensing characteristic to flow property measurements in automotive engines, this paper investigates the feasibility of detecting the start and end of a pulsating flow and its fluid characteristics using an IPMC-beam-based sensor. A dynamic model is developed for the IPMC beam under the flow. The model consists of multiple rigid elements connected by rotational springs and, under suitable conditions, has a closed-form solution that enables efficient estimation of fluid properties and flow parameters with the least-squares minimization approach. The proposed fluid estimation scheme is validated using experimental results with different fluid media, and it is found that the estimated fluid drag coefficients (highly correlated with fluid viscosity) have good agreement with their actual values. This is very important for automotive applications where the characteristics of the fuel blend (such as gasoline and ethanol) need to be identified in real time.**

***Index Terms*—Dynamic model, flow sensing, fluid property estimation, ionic polymer–metal composite (IPMC), least-squares minimization, parameter estimation.**

I. Introduction

In order to improve engine fuel efficiency with reduced exhaust emissions, advanced sensor technologies are widely used for engine management systems (EMS). Prime examples of advanced sensors used in EMS are the mass air flow (MAF), manifold air pressure, in-cylinder ionization, and exhaust oxygen sensors. The MAF in the engine intake manifold and the exhaust oxygen fraction before the three-way catalytic converter are used to control the fuel injection quantity to meet the desired air-to-fuel ratio requirement at the given engine load and speed condition, while the in-cylinder ionization sensor is used to provide the in-cylinder combustion information for feedback control [1], [2]. The existing flow sensors, especially the pulsating flow sensors, operate based upon the Coriolis effect, gear-type positive displacement, piston displacement, ultrasonic measurement, or pressure increase [3]. These technologies are capable of providing accurate laboratory-grade measurements in a well-controlled environment but not suitable to be used in the production environment such as engine fuel systems.

With the application of the biofuel (such as ethanol and biodiesel) in the horizon, detecting the fuel flow and contents (e.g., blend fraction of gasoline and ethanol) becomes a critical technology for maximizing the engine efficiency with reduced emissions [3], [4]. This is because the combustion characteristics are quite different for different fuel contents. One approach to the estimation of biofuel contents is to measure the fluid viscosity or drag coefficient since different biofuel blends have distinct viscosity values. It is desirable to obtain such measurements *in situ* and in real time. A key obstacle preventing existing lab-grade sensors from being used *in situ* is their sizes, calling for new, miniaturized flow sensors that are amenable to the integration with engine fuel systems. With the advances in new materials and microfabrication technologies, microflow sensors have been developed based on a number of transduction principles, such as hot-wire anemometry [5], piezoresistivity [6], and capacitance change [7]. Miniaturized strain gages could also be potentially integrated with a beam structure [8], [9] for flow measurement.

In this paper, we propose the use of an ionic polymer–metal composite (IPMC) beam and a model-based estimation algorithm as a potential approach to *in-situ* measurement of flow properties. IPMC materials have intrinsic sensing and actuation characteristics [10], [11]. As illustrated in Fig. 1, an IPMC has three layers, with an ion-exchange polymer membrane sandwiched by metal electrodes. Inside the polymer (negatively charged) anions covalently fixed to polymer chains are balanced by mobile (positively charged) cations. Deformation under a mechanical perturbation redistributes the cations, producing a detectable electric signal (e.g., short-circuit current) that is well correlated with the mechanical stimulus. Many researchers have studied the fabrication [12]–[14], characterization, and modeling [15]–[20] of IPMC sensors and actuators. There has also been proof-of-concept exploration of using IPMCs as mechanical sensors for force, pressure, displacement, and velocity measurement in medical applications, structural health monitoring, and robotics [21]–[26]. Recent years have seen significant interest in using IPMC materials for underwater actuation [8], [27]–[34], sensing [21], [24], and energy harvesting [35], [36].

Manuscript received April 15, 2011; revised September 11, 2011 and December 22, 2011; accepted March 27, 2012. Date of publication May 4, 2012; date of current version January 18, 2013. Recommended by Technical Editor G. Schitter. This work was supported in part by the National Science Foundation under Grant ECCS 0547131 and in part by the Office of Naval Research under Grant N000140810640 (Program Manager Dr. T. McKenna).

X. Chen is with the Department of Mechanical Engineering, Michigan State University, East Lansing, MI 48824 USA (e-mail: chenxuef@msu.edu).

G. Zhu is with the Department of Mechanical Engineering and the Department of Electrical and Computer Engineering, Michigan State University, East Lansing, MI 48824 USA (e-mail: zhug@msu.edu).

X. Yang is with Delphi Automotive PLC, Troy, MI 48098 USA (e-mail: xiaojian.yang@delphi.com).

D. L. S. Hung is with the University of Michigan–Shanghai Jiao Tong University Joint Institute, Shanghai 200240, China (e-mail: dhung@sjtu.edu.cn).

X. Tan is with the Department of Electrical and Computer Engineering, Michigan State University, East Lansing, MI 48824 USA (e-mail: xbtan@egr.msu.edu).

Color versions of one or more of the figures in this paper are available online at http://ieeexplore.ieee.org.

Digital Object Identifier 10.1109/TMECH.2012.2194300

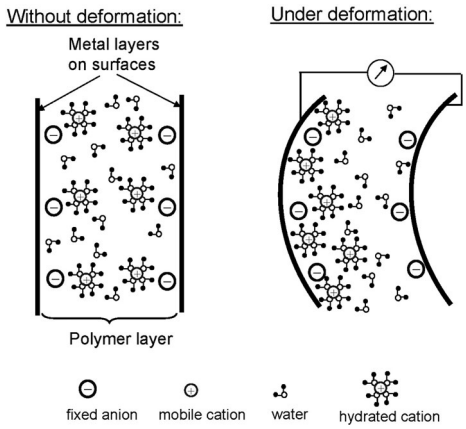

Fig. 1. Illustration of the sensing mechanism of the IPMC material.

We have chosen the IPMC material for flow sensing in this study for several reasons. First, IPMC has direct mechanosensory property, which minimizes the complexity in both the sensor construction and the readout circuit. For example, its readout circuit is much simpler than that required for capacitive flow sensing. Low mechanical and electrical complexity in sensor construction will facilitate the adoption of IPMC in practical applications such as engine fuel systems. Another advantage related to the direct mechanosensory property is the relative ease in modeling the sensor beam dynamics, since we only need to consider a uniform IPMC beam. In contrast, a strain-gage-based flow sensor will typically require embedding the gage in another structural beam, and such a hybrid structure will entail much more complex modeling, which hinders efficient model-based parameter estimation as proposed in this paper. Another advantage of IPMC sensors is that, unlike hot-wire or piezoresistive sensors, they automatically capture the flow polarity. Finally, the softness of IPMC material allows it to respond to small flows and thus attain high measurement sensitivity.

This paper focuses on the potential application of IPMC beams to detecting the start and end of pulsating flows as well as their fluid media characteristics in internal combustion engines. This application requires IPMC beams to respond to various fluid media differently. Therefore, a series of experiments has been designed and conducted to study the characteristics of IPMC beams oscillating in different fluids. The test results show that the IPMC sensor output (short-circuit current) varies as the fluid medium changes, which indicates that the proposed IPMC sensor is able to distinguish different types of fluid media.

In order to extract flow information and fluid properties from the IPMC sensor output, an accurate dynamic model is required for an IPMC beam oscillating in a fluid medium. Modeling of the IPMC beam dynamics has been studied in the context of actuation [30]–[33]. To fully capture the flexible beam dynamics, an infinite-dimensional model is generally required. For practical implementation purposes, however, a finite-dimensional model is desirable. The latter can be achieved by considering the first few dominant vibration modes [30]–[32], or approximating a flexible beam with multiple, serially connected rigid elements [37]–[39]. While linear beam models are only applicable to small deformations, the multisegment approach can effectively address large deformations with low computational complexity [39]. In addition, comparing to the mode summation-based method [30], the latter approach can more easily accommodate nonlinear force terms such as the drag. Therefore, we have adopted the multisegment modeling approach in this paper.

Under appropriate conditions, we show that there exists a closed-form solution for the beam dynamics, and the solution is linear with respect to the fluid property (product of drag coefficient and fluid density) that we are interested in estimating. The correlation of the IPMC sensor output to the beam dynamics is provided in [16], where one can see that the sensor's output signal is approximately proportional to the beam tip velocity when the oscillation frequency is relatively low. Based on the solution for the beam tip velocity, a least-squares minimization procedure is taken to obtain the fluid property estimate, which is readily computed based on the measured IPMC sensing current. We have applied the approach to estimate the properties of different fluid media in pulsating flows, and the identified parameters demonstrate good agreement with their actual values.

The rest of this paper is organized as follows. In Section II, we present the IPMC sensing characteristics under different fluid media. In Section III, the dynamic model for the IPMC beam is described. The parameter estimation approach using the least-squares minimization is developed in Section IV, and experimental results are presented in Section V. Conclusion and other discussions are provided in Section VI.

II. IPMC Sensor Characteristics in Flows

In this section, a series of experiments is performed to study the sensing behavior of an IPMC beam associated with a pulsating flow. We first describe the method for sensor fabrication and signal conditioning, and then present the results on characterizing the IPMC beam dynamics and its sensing response using high-speed imaging analysis. Finally, we show the IPMC sensor responses in pulsating flows of several different fluid media.

A. IPMC Sensor: Fabrication and Sensing Circuit

The IPMC used in this study was fabricated with Nafion-117, a commercial ion-exchange material from DuPont, by following the general ion-exchange and electroless electrode plating processes described in [13]. First, oxygen and argon plasma treatment was applied to roughen the surface of the Nafion film [40], followed by cleaning with boiling acid (HCl) and then with boiling deionized water (*sample preparation*). After these preparation steps, the sample was placed in $[Pt(NH_3)_4]Cl_2$ for over 3 h to incorporate the platinum complex cations into the polymer (*ion-exchange*). Then, we applied the reducing agent $NaBH_4$ to the membrane in a water bath of 60 °C, which reduced the platinum complex ions to platinum near the membrane surfaces (*electrode plating*). The ion-exchange and electrode plating processes were repeated several times until the electrodes were sufficiently strong and thick, as indicated by the surface resistance. The final thickness of the IPMC was about 250 μm. Samples of desired lateral dimensions were then cut with a

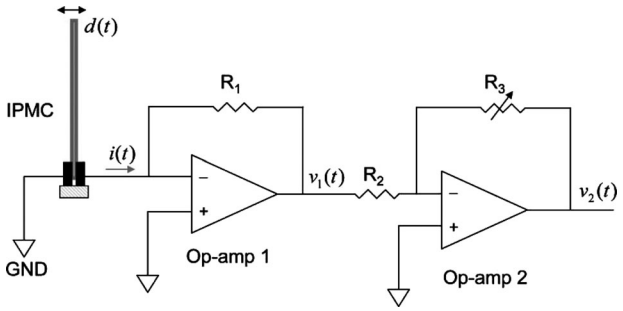

Fig. 2. Schematic of the circuit for measuring short-circuit current output of an IPMC sensor.

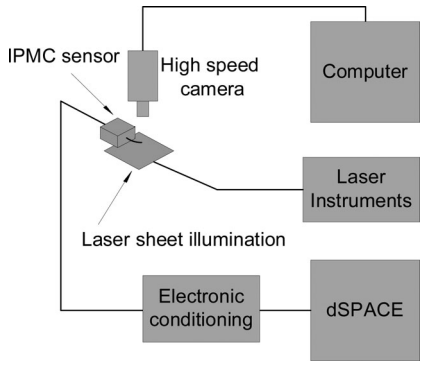

Fig. 3. Schematic of the high-speed imaging system for characterizing IPMC beam behavior.

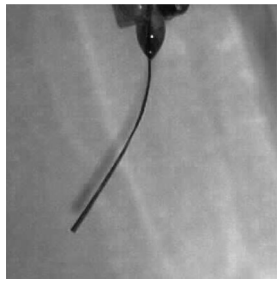

Fig. 4. IPMC cantilever beam used in high-speed imaging analysis.

razor. Little prebending, if any, was observed for the samples used in the experiments.

Fig. 2 shows the schematic of the circuit used to measure the short-circuit current of an IPMC sensor. The circuit uses a two-tier amplification scheme. The first operational amplifier (op-amp) converts the short-circuit current into a voltage, while the second op-amp provides gain adjustment through a tunable resistor. A low-noise, low-bias precision op-amp (OPA 124 from Texas Instruments) is adopted for the first-tier amplification, to reduce both the noise and the spurious dc bias in the sensor output. The measured spurious dc bias was about 0.0054 μA, which was negligible comparing to the actual sensing signals (order of μA) in our work. For op-amp2 in Fig. 2, LM 324 from National Semiconductor is used. The output $v_2(t)$ is related to the current signal $i(t)$ via $v_2(t) = (R_3 R_1/R_2)\, i(t)$. The components we used have the following values: $R_1 = 470$ kΩ, $R_2 = 10$ kΩ, and R_3 is adjustable from 0 to 50 kΩ.

B. High-Speed Imaging-Based Characterization

Fig. 3 shows the schematic of the setup for the high-speed imaging system. A high-speed camera (Photron, Model Fastcam APX RS) was used to record the horizontally vibrating IPMC beam at the rate of 10 000 frames/s. A high-repetition pulsed copper vapor laser (Oxford Lasers, Model LS20–50) was fired to illuminate the beam vibration. The visible laser illumination was directed to the IPMC beam via a fiber-optic cable. The tip displacement of the IPMC beam was extracted from the images using an Optimas image processing analysis software. The sensor output response was taken from the short-circuit current measured between the two electrodes of the IPMC beam. A dSPACE system (dSPACE, DS1104) was used for data acquisition and processing.

Fig. 4 shows the top view of a rectangular IMPC sample (long edge facing up) in the air medium. The dimensions of the beam were 26.9 mm $\times$ 4 mm $\times$ 0.25 mm (length $\times$ width $\times$ thickness). One end of the beam was securely cramped by a fixture, allowing the other end to freely vibrate. The cantilevered beam was initially rested at its default position along the beam axis. Then, it was perturbed manually with about 60° clockwise from its default position. As soon as the beam was released from that position, it oscillated around its base similar to a pendulum swinging around its pivot point. The entire swinging motion was recorded until it gradually returned back to its default position.

Fig. 5 shows the snapshot images of the IPMC beam in a time sequence after it was released (at $t = 0$ s), between 0.1 and 0.4 s as the beam vibrated in stagnant air. Also shown in the figure are the trajectories of the tip displacement extracted from the images and the signal obtained by integrating the IPMC sensing current output. The period of the oscillation was about 0.044 s. It is evident that the beam was highly flexible under free vibrations. Due to the slight dissipation in air and the damping in the beam, the peak displacement slowly diminished until the beam finally returned to its rest position; the peak of the integrated short-circuit current decreased in a similar fashion as the amplitude of the oscillation diminished over time. It can be observed that the integrated short-circuit current correlates very well with the beam tip displacement. This confirms that, at relatively low frequencies, the tip velocity of the IPMC beam can be approximately related to the current output through a static gain, as implied by the physics-based dynamic model for IPMC sensors [16].

C. IPMC Responses in Different Fluid Media

Fig. 6 shows the flow sensor assembly in which an IPMC beam was securely fixed to an adaptor for use in a rigid flow channel. The free length of the IPMC beam was 10 mm. The beam was 4 mm wide and 0.25 mm thick.

Fig. 7 shows the schematic of the experimental setup for characterizing the sensor responses in different fluid media. The bending direction of the beam was aligned with the direction of the pressurized pulsating flow. The IPMC sensor was located at the inlet of the solenoid control valve. The ON–OFF solenoid

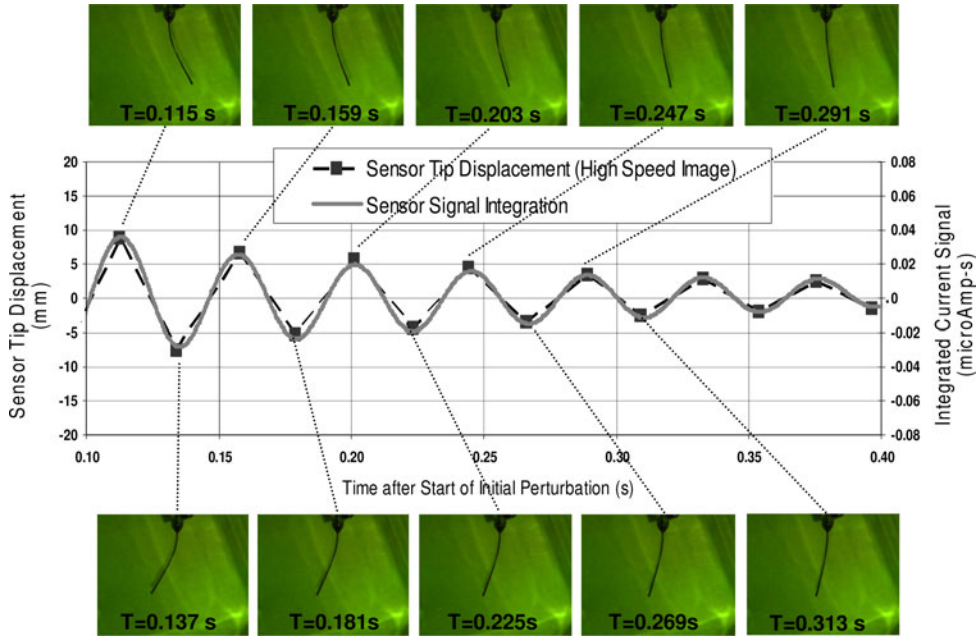

Fig. 5. Tip displacement captured by the high-speed imaging system and the integrated short-current signal of the IPMC sensor vibrating in air.

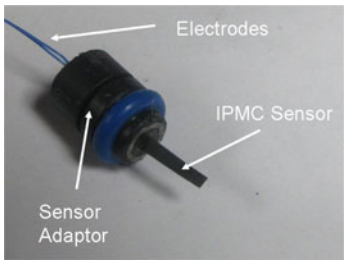

Fig. 6. IPMC beam in a sensor assembly.

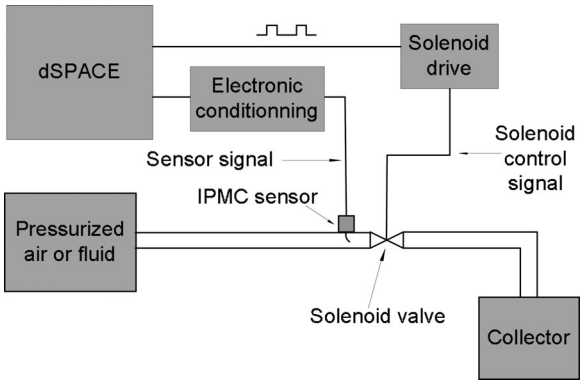

Fig. 7. Schematic of the experimental setup for characterizing IPMC sensor responses in different fluid media.

control signal shown in Fig. 7 was used to generate the pulsating flow to excite the IPMC sensor.

Three fluid media, nitrogen gas, distilled water, and n-Heptane, were used in the experiments due to their distinct fluid properties such as density and viscosity. Note that n-Heptane is a single-constituent hydrocarbon liquid typically substituted for gasoline in bench testing of gasoline fuel system components,

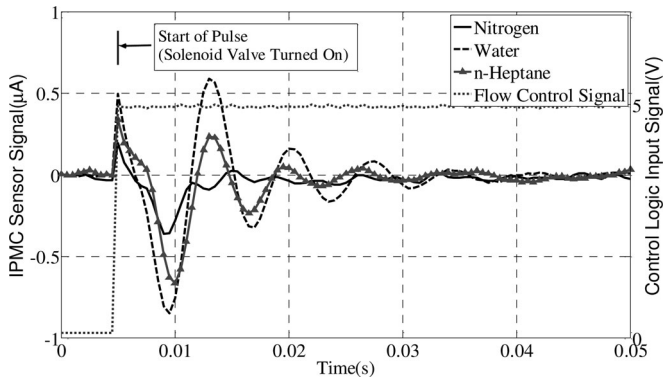

Fig. 8. IPMC sensor responses after the start of the flow pulse.

and both its density and viscosity are in the mid-range between those of nitrogen gas and distilled water.

Fig. 8 shows the responses of the IPMC sensor stimulated by three different fluid media after the solenoid valve was opened. The fluid pressure was regulated at 207 kPa and the solenoid pulse duration (pulsating flow duration) was set to 100 ms. The "Start of Pulse" in the figure indicated the instant when the solenoid was energized (i.e., valve opened). The key information provided in Fig. 8 is that the IPMC beam signals were quite distinct under the three fluid media. In particular, the peak amplitude and the decay of the damped oscillations were highly correlated with the differences in the fluid media. The signal magnitude was the largest for water, which has the highest density and viscosity among the three fluids. The IPMC sensor responses following the end of pulsating flow (by deactivating the solenoid valve) also demonstrated different characteristics for the tested fluid media, as shown in Fig. 9.

Besides the fluid properties, the fluid injection pressure (or flow rate) is a key parameter for internal combustion engines.

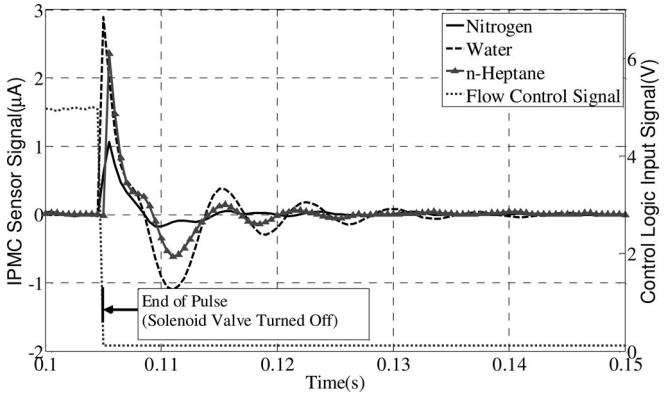

Fig. 9. IPMC sensor responses following the end of the flow pulse.

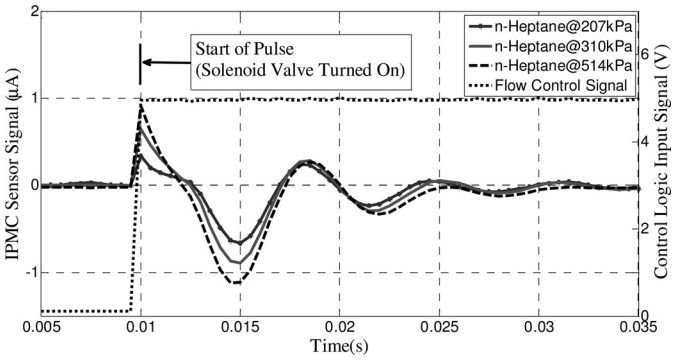

Fig. 10. IMPC sensor responses to n-Heptane flow under three fluid pressures.

Fig. 10 shows the IPMC sensor response to an n-Heptane flow at three fluid pressures of 207, 310, and 514 kPa. These pressures correspond to typical conditions found in a port fuel injection system of gasoline engines. While the signals demonstrated similar damping behaviors for the three pressures, their amplitudes were different—the higher the pressure, the larger the signal amplitude. This is reasonable because the fluid flow rate directly impacts the driving force on the IPMC beam movement and thus the sensor output. Figs. 8–10 indicate that both the amplitudes and the decay characteristics of the IPMC sensor output carry useful information about the flow properties. Note that the sensor signal amplitudes and the decay characteristics shown in Fig. 10 provide a strong indication that an IPMC sensor is not only capable of characterizing pulsating flows, but also possibly capturing various flow conditions.

D. IPMC Beam Responses to Cyclic Flows

In addition to reacting to pulsating flows with different fluid media and flow rates, another advantage of an IPMC flow sensor is its ability to capture the pulse-to-pulse variations between consecutive events initiated by the solenoid valve. Fig. 11 shows the sensor response to two consecutive pulsating events of the water flow at 270 kPa. In this test, the solenoid valve was open for 100 ms and the pulse period was also set to 100 ms, providing a 50% duty-cycle pulsating flow. As the solenoid valve was energized by a transistor–transistor logic input signal, the sensor movement was induced by the pulsating fluid movement,

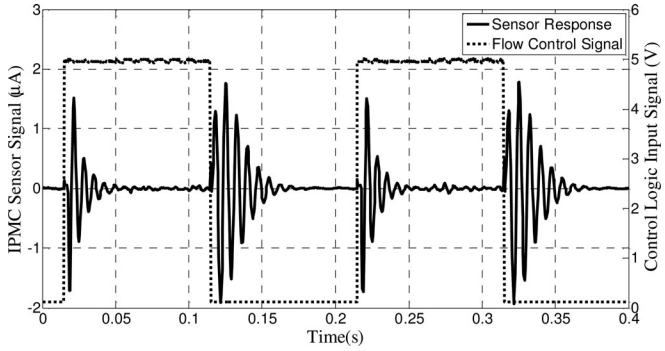

Fig. 11. IPMC sensor response to two consecutive pulses of water flow.

resulting in distinct vibration signals immediately after the rising and falling edges of the logic pulse, respectively. It can be clearly seen that the sensor provides fairly repeatable signal corresponding to both pulse events. The information embedded in the signal slightly after the rising edge and the falling edges of the consecutive pulses could be useful for interpreting the pulse-to-pulse variations of the pulsating flow. This type of information is very critical to engine fuel flow control and calibrations which directly influence combustion stability. Currently high-fidelity measurement of the pulse-to-pulse flow variation is only available through a laboratory test bench. With the help of the IPMC flow sensor, it might be possible to measure it in the vehicle environment.

In summary, based upon the aforementioned experimental results, IPMC holds strong promise for measuring pulsating flow characteristics in internal combustion engines, including flow start and end instants, flow rate, pulse-to-pulse variations, and fluid media properties. In the following section, we will discuss a multisegment model for the IPMC beam dynamics in a fluid medium, which will be useful for estimating fluid characteristics based on the IPMC sensor output.

III. Dynamic Model of an IPMC Beam in Fluid Flow

In order to effectively describe the dynamic responses of an IPMC beam interacting with a fluid flow, a multisegment dynamic model is adopted in this paper. Fig. 12 illustrates the beam model with N rigid-body elements. The elements have equal length, and each is linked with its neighbor elements through joints modeled by a rotational spring K_i and a linear rotational damper H_i, where the index i denotes the ith element. The damper collectively models the internal damping of the IPMC beam and the hydrodynamic damping due to the interaction with the surrounding fluid [30]. We have not considered the nonlinear damping effect in the interest of deriving an efficient estimation algorithm for real-time applications. We will further discuss this issue in Section VI. The drag force F_{Di} due to the surrounding medium can be modeled as a lumped load applied at the element center of mass.

Fig. 13 shows the free body diagram for one element, where (x, y) are the coordinates in the inertial frame. For each element, the governing equation can be written in the following form

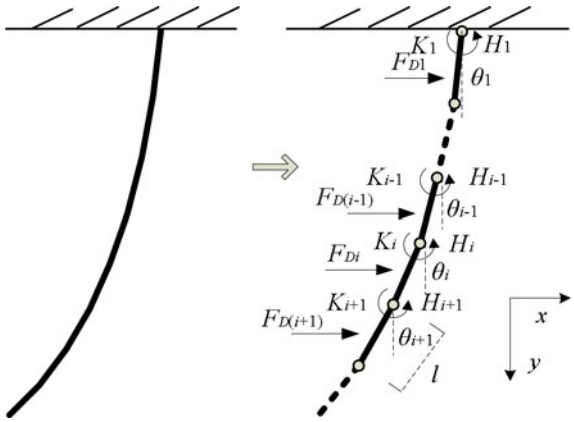

Fig. 12. Cantilever beam modeled by a finite number of rigid elements.

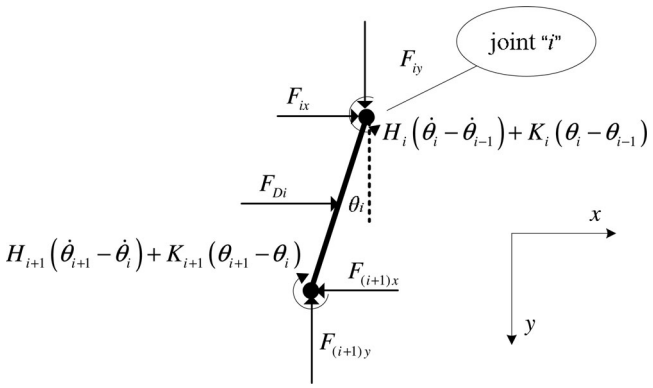

Fig. 13. Free body diagram of the *i*th beam element.

based upon Newton's law:

$$\begin{aligned} J_i\ddot{\theta}_i &+ H_i\left(\dot{\theta}_i - \dot{\theta}_{i-1}\right) + K_i\left(\theta_i - \theta_{i-1}\right) \\ &- H_{i+1}\left(\dot{\theta}_{i+1} - \dot{\theta}_i\right) - K_{i+1}\left(\theta_{i+1} - \theta_i\right) \\ &= F_{iy}\sin\theta_i\frac{l}{2} + F_{ix}\cos\theta_i\frac{l}{2} \\ &+ F_{(i+1)y}\sin\theta_i\frac{l}{2} + F_{(i+1)x}\cos\theta_i\frac{l}{2}, \quad (i = 1, \ldots, N) \end{aligned} \tag{1}$$

where J_i is the moment of inertia for the *i*th element, l is the length of the beam element, F_{ix} and F_{iy} are the reaction forces at the *i*th node in the *x*- and *y*-directions, respectively, and $F_{(i+1)x}$ and $F_{(i+1)y}$ are defined similarly for the $(i+1)$th node. Note that, from Newton's law, the translational motion satisfies the following equations:

$$m_i \cdot a_{ix} = F_{Di} + F_{ix} - F_{(i+1)x} \tag{2}$$

$$m_i \cdot a_{iy} = F_{iy} - F_{(i+1)y} \tag{3}$$

where m_i is the effective mass of beam element *i*, as defined later in (11), and a_{ix} and a_{iy} are the accelerations in *x*- and *y*-directions, respectively, at the center of the mass for element *i*. To facilitate the derivation of an efficient estimation algorithm for real-time applications, we assume small angular displacements in this study, so that

$$\sin\theta_i \approx \theta_i,\ \cos\theta_i \approx 1, \quad i = 1, 2, \ldots, N. \tag{4}$$

Note that the approximation made in (4) leads to a maximum error of 1.5% when the beam angle is less than or equal to 10° (0.17 rad). With this assumption, both a_{ix} and a_{iy} can be approximated by the following equations:

$$a_{ix} = \sum_{j=1}^{i-1}\ddot{\theta}_j l + \frac{1}{2}\ddot{\theta}_i l, \quad i = 1, 2, \ldots, N \tag{5}$$

$$a_{iy} = 0, i = 1, 2, \ldots, N. \tag{6}$$

Note that since $F_{(N+1)y}$ is zero, we have $F_{iy} = 0$, $i = 1, 2, \ldots, N$, from (3) and (6). On the other hand, from (2) and (5), F_{ix} in (1) can be solved as a linear combination of F_{Dj} and $\ddot{\theta}_j$, $j = 1, 2, \ldots, N$, with $F_{(N+1)x} = 0$.

The drag force F_{Di} applied to each element is exerted by the surrounding medium, and it can be expressed as

$$F_{Di} = b \cdot l \cdot C_D \cdot \rho \cdot \frac{\hat{V}_i^2}{2} \tag{7}$$

where b is the beam element width, C_D is the drag coefficient, ρ is the fluid density, and $\hat{V}_i$ is the relative beam velocity with respect to the fluid at the center of the element. Note that $\hat{V}_i = V_0 + V_{xi}$, where V_0 is the fluid velocity, and V_{xi} is the *x*-direction component of the beam element linear velocity V_i at its center of mass. Again, assuming that θ_i is relatively small, we can approximate V_{xi} by V_i..

The moment of inertia J_i, rotational stiffness K_i, and damping coefficient H_i can be expressed in terms of the beam dimensions, and the properties of the beam material and the fluid

$$J_i = J_e = \frac{m_i \cdot l^2}{12} \tag{8}$$

$$K_i = K_e = \frac{\gamma \cdot b \cdot c^3}{12l} \tag{9}$$

$$H_i = H_e = \xi \cdot 2\sqrt{J_i \cdot K_i} = \xi \cdot 2\sqrt{J_e \cdot K_e} \tag{10}$$

where m_i is the effective mass for element *i*, c is the beam element thickness, γ is the (effective) Young's modulus of IPMC material, and ξ is the critical damping ratio accounting for both material damping and hydrodynamic damping. The effective mass m_i represents the sum of the actual mass of element *i* and the added mass for this element due to beam–fluid interactions [30], [43], and it can be expressed as

$$m_i = \rho_e blc \tag{11}$$

where ρ_e represents the effective density of the beam, which depends on the material density, fluid density, and beam geometry. Note that since all the beam elements are identical, they have the same moment of inertia J_e, stiffness K_e, and the damping coefficient H_e.

We can rewrite (1) in a compact matrix form

$$J \cdot \ddot{\theta} + H \cdot \dot{\theta} + K \cdot \theta = \Gamma \tag{12}$$

where *J, H*, and *K* are matrices of moments of inertia, damping coefficients, and spring constants, respectively. For the

N-element beam model, these matrices are expressed as

$$J = \times \begin{bmatrix} 12(N-1)+4 & 12(N-2)+6 & \cdots & \cdots & 18 & 6 \\ 12(N-2)+6 & 12(N-2)+4 & \cdots & \cdots & 18 & 6 \\ \vdots & \vdots & \ddots & & \vdots & \vdots \\ \vdots & \vdots & & \ddots & 18 & 6 \\ 18 & 18 & \cdots & 18 & 16 & 6 \\ 6 & 6 & \cdots & 6 & 6 & 4 \end{bmatrix} J_e \tag{13}$$

$$H = \begin{bmatrix} 2H_e & -H_e & & & \\ -H_e & 2H_e & \ddots & & \\ & \ddots & \ddots & \ddots & \\ & & \ddots & 2H_e & -H_e \\ & & & -H_e & H_e \end{bmatrix} \tag{14}$$

$$K = \begin{bmatrix} 2K_e & -K_e & & & \\ -K_e & 2K_e & \ddots & & \\ & \ddots & \ddots & \ddots & \\ & & \ddots & 2K_e & -K_e \\ & & & -K_e & K_e \end{bmatrix}. \tag{15}$$

The angular displacement vector θ and the fluid flow-induced torque vector Γ are expressed as

$$\theta = \begin{bmatrix} \theta_1 \\ \vdots \\ \theta_i \\ \vdots \\ \theta_N \end{bmatrix}, \Gamma = \frac{l}{2} \begin{bmatrix} F_{D1} + 2\sum_{j=2}^{N} F_{Dj} \\ \vdots \\ F_{Di} + 2\sum_{j=i+1}^{N} F_{Dj} \\ \vdots \\ F_{DN} \end{bmatrix}. \tag{16}$$

IV. Least-Squares Fluid Parameter Identification

Assume that all the IPMC beam model parameters defined in (13)–(15) are available. We further assume that the fluid flow velocity V_0 in (16) is known; in practice, this value could be determined in a number of ways, e.g., based on the applied fluid pressure. We can rewrite (12) into the following state-space form, where the product of remaining unknown parameters C_D and ρ appears linearly in the driving term

$$\begin{aligned} \dot{x} &= Ax + Bu, \quad u = \bar{V} C_D \rho \\ y &= Cx, \quad y = \dot{\theta}_N \end{aligned} \tag{17}$$

where

$$x = \begin{bmatrix} \theta \\ \dot{\theta} \end{bmatrix}, \quad A = \begin{bmatrix} 0_{N\times N} & I_{N\times N} \\ -J^{-1}_{N\times N} \times K & -J^{-1}_{N\times N} \times H_{N\times N} \end{bmatrix}$$

$$B = \begin{bmatrix} 0_{N\times N} \\ J^{-1}_{N\times N} \times Q_{N\times N} \end{bmatrix}, \quad C = [\, 0_{1\times(N-1)} \quad 1 \,]$$

where $I_{N\times N}$ is an identity matrix and

$$Q_{N\times N} = \frac{bl^2}{2} \begin{bmatrix} 1/2 & 1 & \cdots & 1 & 1 \\ 0 & 1/2 & \cdots & 1 & 1 \\ \vdots & \vdots & \ddots & \vdots & \vdots \\ 0 & 0 & \cdots & 1/2 & 1 \\ 0 & 0 & \cdots & 0 & 1/2 \end{bmatrix}$$

$$\bar{V} = \begin{bmatrix} (V_0+V_1)^2 \\ \vdots \\ (V_0+V_i)^2 \\ \vdots \\ (V_0+V_N)^2 \end{bmatrix}.$$

Note that the velocity V_i at the center of element *i* and the beam tip velocity V_{tip} satisfy the following equations:

$$V_i = l\dot{\theta}_i/2 + \sum_{j=1}^{i-1} l\dot{\theta}_j \tag{18}$$

$$V_{\text{tip}} = \sum_{j=1}^{N} l\dot{\theta}_j. \tag{19}$$

As discussed in Section II, when the vibration frequency is relatively low, the short-circuit current signal i_{short} from the IPMC sensor can be related to the beam tip velocity V_{tip} through a static gain as

$$V_{\text{tip}} = \eta \cdot i_{\text{short}} \tag{20}$$

where the gain η can be determined with the formulas presented in [16] or obtained experimentally.

From (14) and (15), the damping matrix *H* is proportional to the stiffness matrix *K*, i.e.,$H = \beta K$, where β is a scalar. The mode frequencies in system (12) can be obtained by using Rayleigh damping theory [41]. System (12) can be transformed into its modal coordinates

$$\ddot{q} + \bar{H}\dot{q} + \bar{K}q = P^T\Gamma \tag{21}$$

where $q = P^{-1}\theta$ is the angular displacement vector in the modal coordinates, and $\bar{H} = P^T HP$ and $\bar{K} = P^T KP$ are diagonalized damping and stiffness matrices, respectively. The column vectors, $P_i (i = 1, 2, \ldots, N)$, of the coordinate transformation matrix, $P = [\, P_1, \quad \ldots, \quad P_i, \quad \ldots, \quad P_N \,]$, is the orthonormal mode shape vectors satisfying the following conditions:

$$(K - \omega_i^2 J)P_i = 0 \text{ and } P_i^T JP_i = 1, \quad i = 1, 2, \ldots, N \tag{22}$$

where ω_i is the *i*th mode frequency. Recall that we are concerned with pulsating flows in this paper. Therefore, within each pulse, the IPMC beam is subject to a constant flow following the initial impact, which implies that the first mode response $P_1 = [\, p_{11}, \quad \ldots, \quad p_{i1}, \quad \ldots, \quad p_{N1} \,]^T$ dominates the beam vibrations. If higher frequency modes are excited by the initial impact, the responses associated with those modes will be damped out much faster than that of the first mode, in which case one can use the output data beyond the initial impact for parameter estimation. With these considerations, we derive the

following relationships between the angular velocities:

$$\frac{\dot{\theta}_1}{p_{11}} = \cdots = \frac{\dot{\theta}_i}{p_{i1}} = \cdots = \frac{\dot{\theta}_N}{p_{N1}}. \tag{23}$$

Consequently, from (18) and (19), the velocity V_i for element i can be expressed in terms of the beam tip velocity V_{tip}

$$V_i = \frac{\sum_{j=1}^{i-1} p_{j1} + \frac{1}{2}p_{i1}}{\sum_{j=1}^{N} p_{j1}} V_{\text{tip}}. \tag{24}$$

For practical implementation purposes, we can convert the continuous-time model (17) to the discrete-time version

$$\begin{aligned} x(k+1) &= \hat{A}x(k) + \hat{B}u(k) \\ y(k) &= \hat{C}x(k) \end{aligned} \tag{25}$$

for a given sampling period T_s, where $\hat{A} = e^{AT_s}$,$\hat{C} = C$, and $\hat{B} = \int_0^{T_s} e^{A\sigma} B_c d\sigma$. The solution to (25) can be obtained as

$$\begin{aligned} x(k) &= \hat{A}^k x(0) + \sum_{j=0}^{k-1} \hat{A}^{k-j-1} \hat{B} \bar{V}(j) C_D \rho \\ y(k) &= \hat{C}x(k). \end{aligned} \tag{26}$$

Let the initial condition of the state be $x(0) = x_0$. The following equation can be obtained based upon (26):

$$\begin{aligned} \bar{y} &= \begin{bmatrix} y(1) \\ y(2) \\ \vdots \\ y(n) \end{bmatrix} = \begin{bmatrix} \hat{C}\hat{A}^1 & \hat{C}\hat{A}^0\hat{B}\bar{V}(0) \\ \hat{C}\hat{A}^2 & \hat{C}\sum_{j=0}^{1} \hat{A}^{1-j}\hat{B}\bar{V}(j) \\ \vdots & \vdots \\ \hat{C}\hat{A}^n & \hat{C}\sum_{j=0}^{n-1} \hat{A}^{n-j-1}\hat{B}\bar{V}(j) \end{bmatrix} \begin{bmatrix} x_0 \\ C_D\rho \end{bmatrix} \\ &= \Phi(n) \begin{bmatrix} x_0 \\ C_D\rho \end{bmatrix} \end{aligned} \tag{27}$$

where n is the number of signal data points selected for identification. Note that the system matrices $(\hat{A}, \hat{B}, \hat{C})$ are known, and the velocity vector $\bar{V}$, as defined following (17), can be calculated using (20) and (24). Therefore, the matrix $\Phi(n)$ can be obtained based upon the IPMC sensor output. To estimate the fluid property parameter $C_D\rho$ (product of the drag coefficient and fluid density), we seek the solution that minimizes the squared error

$$\left\| \bar{y} - \Phi(n) \begin{bmatrix} x_0 \\ C_D\rho \end{bmatrix} \right\|_2. \tag{28}$$

The corresponding solution can be readily computed as

$$\begin{bmatrix} x_0 \\ C_D\rho \end{bmatrix} = [\Phi^T(n)\Phi(n)]^{-1}\Phi^T(n)\bar{y}. \tag{29}$$

V. Experimental Results on Fluid Property Estimation

In this section, we apply the proposed modeling and estimation approach to estimate the fluid property parameter $C_D\rho$ for two fluid media (water and n-Heptane) based upon the IPMC sensor output signals shown in Figs. 8 and 9. The number of rigid elements in the model impacts both modeling accuracy and computational complexity; a higher number of elements leads to more accurate modeling but entails higher computational cost.

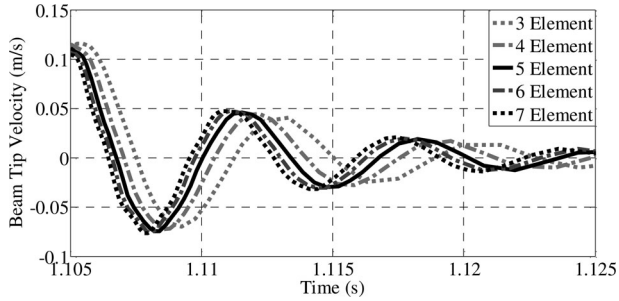

Fig. 14. Convergence of the model as the number of beam elements increases.

The number of rigid elements required to achieve certain accuracy in approximating a flexible beam is highly dependent on the geometry and material properties of the beam [42].

Fig. 14 shows the simulated responses of the beam tip velocity following an initial impact, when different values of N are adopted for the number of rigid elements. The beam dimensions used in the simulation were the same as those of the IPMC beam used in the experiments, and other simulation parameters were chosen based on general knowledge about beam and fluid properties. The Simulink Simscape toolbox was utilized for the simulation. It can be observed in Fig. 14 that, as the element number increases, the beam tip velocity trace gradually converges, and that the five-element model achieves a sound tradeoff between modeling accuracy and computational efficiency. Therefore, a model with five rigid elements was adopted in this study.

Before applying the estimation algorithm, we need to identify a few parameters for the beam model. The effective Young's modulus γ of IPMC was calculated based on the measured beam stiffness, following an experimental procedure described in [44]. The width b and the thickness c of the beam were measured directly, and the length l of each beam element was obtained by the measured beam length divided by 5. The gain η relating the beam tip velocity to the IPMC short-circuit current was estimated based on the results from high-speed imaging analysis (see Fig. 5). Finally, the damping ratio ξ and the effective beam density $\rho_e$were identified through curve-fitting, as shown in Fig. 15. In particular, we tuned these two parameters until good agreement was achieved between the simulated beam tip velocity and the measured short-circuit current signal, following the rising edge of the control pulse in a pulsating water flow. These parameters were then used to estimate the fluid property parameter for other cases. Table I lists all the parameters identified for the beam model.

Table II lists the properties of the two fluids (water and n-Heptane), as well as their measured average velocities. Reynolds numbers R_e of the two fluids are obtained as follows [45]:

$$R_e = \frac{V_0 b}{v} \tag{30}$$

where $v$is the kinematic viscosity of the fluid. Based upon the obtained Reynolds number, the actual drag coefficient C_D can be found using [45, Fig. 8.8 and Table VIII.2]. Note that these drag coefficients were obtained with the assumption of a round, cylindrical beam. Since the IPMC beam is rectangular, we have provided a range of values for C_D in Table II.

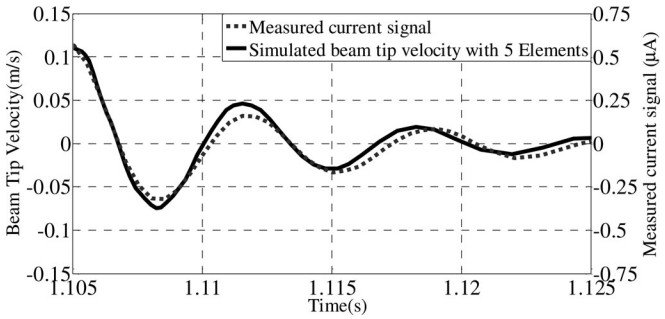

Fig. 15. Identification of ξ and ρ_e through curve-fitting, where the measured IPMC current was taken from the case of a pulsating water flow, following the activation of the solenoid valve.

TABLE I
PARAMETERS OF THE EXPERIMENTAL IPMC BEAM

γ (N/mm²)	ξ	ρ_e (g/cm³)	η (m/s/μA)	l (mm)	b (mm)	c (mm)
500	0.14	3	0.22	2	4	0.25

TABLE II
PARAMETERS OF THE TESTED FLUIDS

Liquid	ρ (g/cm³)	v (mPa·s)	V_0 (m/s)	R_e	C_D
Water	1	1.007×10^{-6}	0.15	595.8	1.1 to 1.3
n-Heptane	0.684	0.564×10^{-6}	0.22	1583.4	0.8 to 1

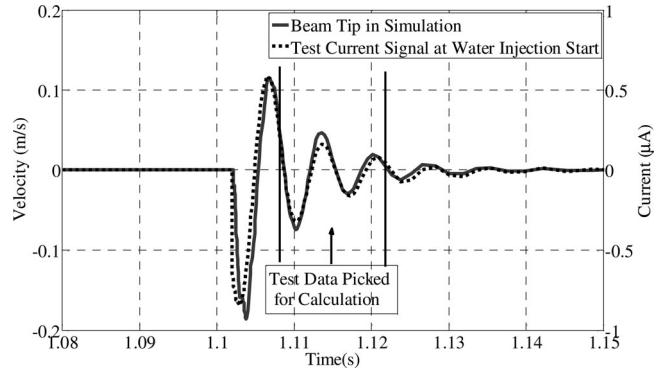

Fig. 16. Selection of signal segment for parameter estimation, for the case where the beam motion was initiated by the start of a water flow pulse.

Next, we will estimate the fluid property parameter $C_D\rho$ for water and n-Heptane using the measured IPMC sensor outputs shown in Figs. 8 and 9 and compare the estimates with the values derived from Table II. The sampling time was 0.5 ms. Fig. 16 shows the IPMC short-circuit current signal following the start of the water flow, and the simulated beam tip velocity based on the parameters ξ, ρ_e, and $C_D\rho$ that were obtained through curve-fitting. Recall that this was how the beam parameters ξ and ρ_e were identified. Due to the large angular displacement at the start of pulse flow, the current signal does not match well the simulated beam tip velocity immediately following the impact, since small displacement was assumed in the modeling process. In order to better identify the fluid property, we focused on a data segment away from the initial impact. The two vertical lines in Fig. 16 depict the time interval for which the sensor data were used for parameter estimation.

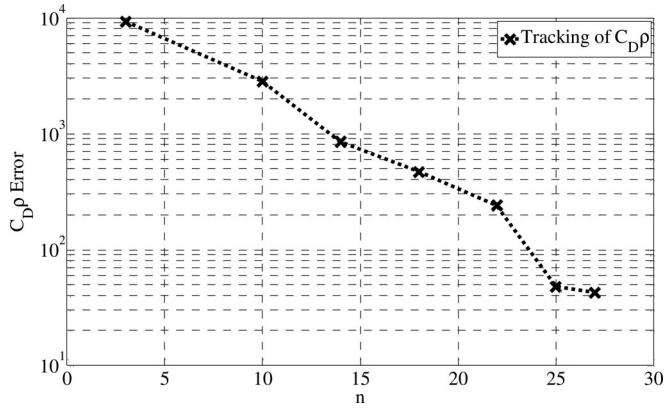

Fig. 17. Estimation error as a function of data length, for the case where the beam motion was initiated by the start of a water flow pulse.

TABLE III
ESTIMATED FLUID PROPERTY PARAMETER $C_D\rho$ FOR WATER AND n-HEPTANE

Injection	Fluid	Calculated $C_D\rho$	Estimated $C_D\rho$
Start	Water	1100-1300	1157.4
End	Water	1100-1300	1137.0
Start	n-Heptane	547.2-684	579.3
End	n-Heptane	547.2-684	613.2

Note that the number n of data points used in parameter identification affects the accuracy of the least-squares estimation. To demonstrate this effect, we took the test data shown in Fig. 16 and performed estimation with data of different length. Fig. 17 shows the estimation error as a function of the signal length n. The estimation error is with respect to the midpoint of the calculated range for $C_D\rho$ shown in Table III. It can be seen that the estimation error drops as the signal length increases. But after the signal length is increased to a certain value, the estimation error converges. This is because it takes a certain number of data points to convey the oscillation characteristics. Therefore, the selection of the test data segment (including the data length) plays an important role in determining estimation accuracy and computational complexity. Fig. 18 shows the selected data segments for parameter estimation for the three other cases. Note that in these cases, ξ and ρ_e identified earlier were used, and the values of $C_D\rho$ were obtained from the least-squares optimization.

The estimated fluid property parameters are summarized in Table III against the calculated ones. Here, the calculated $C_D\rho$ range is obtained based on the data listed in Table II. It can be seen that the identified parameters are very close to their corresponding calculated values. Furthermore, the identified parameters using the data following the start of the pulses are consistent with those based upon the data following the end of the pulses. This is very important for automotive applications of on-board diagnostics and fuel composition detection.

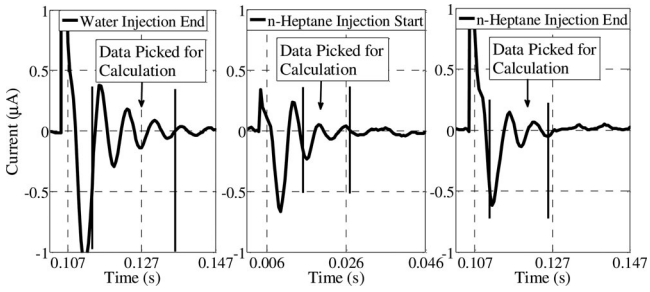

Fig. 18. Selection of signal segments for parameter identification for the other three cases.

VI. Conclusion and Discussion

Motivated by the potential application of the IPMC beam as flow sensors for automotive engines, this paper investigates the feasibility of an efficient algorithm for identifying the fluid properties using the output of an IPMC sensor beam under pulsating flows. A dynamic multisegment model for IPMC beam dynamics was developed and solved analytically. The obtained solution, linear in the parameter of interest (product of drag coefficient and fluid density), was then used to identify the fluid parameter through least-squares minimization, where, again, an analytical solution was readily available. The estimation scheme was applied to pulsating flows of two different media, water and n-Heptane, and the estimated fluid parameters showed good agreement with the true parameters for those media.

Our work has shown the promise of using IPMC for measuring flow conditions and fluid properties in pulsating flows. While the study was motivated by emerging automotive applications (such as detecting the composition of fuel blends), it can be extended and applied to flow sensing in other areas including biomedical systems. One such example could be the measurement of flow characteristics in blood vessels (pulsating flow in nature). On the fabrication side, with the advances being made in lithography-based microfabrication [14], [46], and [47], IPMC sensors can be scaled down to the micrometer range to accommodate the aforementioned applications. On the algorithm side, the dynamic model and the associated estimation scheme proposed in this paper accommodate scaling naturally.

We now discuss several characteristics of IPMC materials as relevant to their proposed use in this paper. The first is the bandwidth of an IPMC sensor. Since the sensing property is enabled by the redistribution of ions under mechanical stimuli, one might be concerned about the IPMC sensing bandwidth (the actuation bandwidth of IPMC is typically below 10 Hz). In fact, the bandwidth of IPMC sensors is sufficiently high for most applications envisioned in this paper. For example, as it can be seen in Figs. 8–11, the output of an IPMC sensor beam that is 10 mm long, 4 mm wide, and 0.25 mm thick can clearly capture the motion of the beam vibrating at about 150 Hz. For property measurement of a flow (especially, a pulsating flow), one can design the geometry of the IPMC beam, so that its resonant frequency is high enough to allow significant mechanical motion in the frequency range of interest. We note, however, that as the sensor is scaled down (e.g., by making it shorter) to obtain high resonant frequencies, the signal conditioning and amplification circuit needs to be properly enhanced to accommodate the generally weaker output from a small sensor.

It should be noted that fabrication of IPMC materials is not fully mature yet. For example, sample properties may have batch-to-batch variations, and material behaviors can change over time. As a result, one will need to calibrate individual sensors and periodically recalibrate them to obtain accurate sensor parameters in practical applications. On the other hand, IPMC fabrication is a very active research area and it is anticipated that, with further development, IPMCs will have much reduced batch-to-batch variation and much improved long-term behavioral stability. Furthermore, the model-based estimation algorithm proposed in this paper exploits salient features (e.g., the damping characteristics) of the beam dynamics, which greatly reduces the importance of the absolute signal amplitude and thus mitigates the impact of the nonideal behavior of IPMCs. We also want to point out that the modeling approach and the estimation algorithm presented in this paper are applicable to other beam-shaped flow sensors and thus not limited to IPMC sensors.

This study has not considered the effect of surrounding fluid media on IPMC physical and mechanosensory properties. This did not seem to have a big impact on this study since, in each experiment, the IPMC sensor had relatively short time in contacting with the fluid. In long-term applications, one will need to address the potential influence of the fluid media on the sensor behavior. One approach is to coat or package the IPMC sensor beam so that it is isolated from the fluid. An alternative is to characterize the mechanical and sensing properties of the IPMC beam in each fluid and incorporate those properties in model-based estimation. In this paper, we have also ignored the phase lag between the IPMC current output and the tip velocity. Such dynamics [16] can be incorporated to improve the estimation accuracy, especially for applications involving high-frequency beam oscillations.

In the interest of obtaining analytical solutions and thus efficient estimation algorithms for real-time applications, we have adopted several approximations and simplifications in the modeling and estimation approach. When offline estimation is acceptable, or when adequate computing power is available, one can consider extending the approach in a few directions, to improve the accuracy in the beam dynamics modeling and in the fluid property estimation.

First, instead of using the multisegment modeling approach presented in this paper, one can consider using nonlinear finite-element methods to solve the nonlinear beam dynamics, which can potentially lead to more accurate solutions. Second, we have assumed a constant added-mass in this paper. In extension, one could incorporate the fluid density dependence of the added mass in the inertia matrix. The resulting estimation problem will be much more sophisticated, but it offers the possibility to simultaneously estimate the fluid density and the drag property. Third, nonlinearities can be included to improve the model fidelity across wider ranges of operating conditions and fluid properties. Besides dropping the small angular displacement assumption, an interesting question to investigate is nonlinear hydrodynamic damping. For example, the Keulegan–Carpenter

(KC) number [48] in our setting was estimated to be about 0.5 and the frequency parameter was about 2400. Nonlinear damping, where the damping coefficient depends on the oscillation amplitude and frequency, could exist for such a combination of KC number and frequency parameter [49]. In our work, nonlinear damping has not been considered, which is partly justified by the fact that in many applications of interest (e.g., estimating a pulsating flow in an engine fuel system), the resulting amplitudes and frequencies of beam oscillations have relatively small variations. For other applications where the vibration characteristics could vary significantly, it will be of interest to examine nonlinear damping.

Finally, we note that, while this paper has focused on the sensing of pulsating flows, IPMC sensors can also be used to measure continuous flows. In the latter setting, the flutter instability of an IPMC beam when the flow speed exceeds critical values can be potentially exploited to extract the flow information. For example, the measurement of the flutter frequency (easily available from IPMC output) can be used to infer either the flow speed (if fluid properties, such as viscosity, are known) or the fluid properties (if the flow speed is known).

REFERENCES

[1] S. Prosser, "Automotive sensors: past, present and future," *J.Phys., Conf. Series*, vol. 76, pp. 012001-1–012001-6, 2007.

[2] G. Zhu, I. Haskara, and J. R. Winkelman, "Stochastic limit control and its application to knock limit control using ionization feedback," in *Proc. SAE 2005 World Congr.*, Tech. Paper 2005-01-0018.

[3] A. Gandhi, M. Meinhart, and S. Ortiz, "A summary of flow metering options for injector characterization," in *Proc. SAE 2009 World Congr.*, Tech. Paper 2009-01-0747.

[4] S. Pace and G. Zhu, "Air-to-fuel ratio and dual-fuel ratio control of an internal combustion engine," in *Proc. SAE 2009 World Congr.*, Tech. Paper 2009-01-2794.

[5] Y. Yang, J. Chen, J. Engel, S. Pandya, N. Chen, C. Tucker, S. Coombs, D. L. Jones, and C. Liu, "Distant touch hydrodynamic imaging with an artificial lateral line," in *Proc. Nat. Acad. Sci.*, vol. 103, no. 50, pp. 18891–18895, 2010.

[6] Y. Yang, N. Nguyen, N. Chen, M. Lockwood, C. Tucker, H. Hu, H. Bleckmann, C. Liu, and D. L. Jones, "Artificial lateral line with biomimetic neuromasts to emulate fish sensing," *Bioinspirat. Biomimet.*, vol. 5, p. 016001, 2010.

[7] A. Dagamseh, T. Lammerink, M. Kolster, C. Bruinink, R. Wiegerink, and G. Krijnen, "Dipole-source localization using biomimetic flow-sensor arrays positioned as lateral-line system," *Sens. Actuators A*, vol. 162, no. 2, pp. 355–360, 2010.

[8] K. Leang, Y Shan, S. Song, and K. Kim, "Integrated sensing for IMPC actuators using strain gages for underwater applications," *IEEE/ASME Trans. Mechatronics*, vol. 17, no. 2, pp. 345–355, Apr. 2012.

[9] A. Fleming and K. Leang, "Integrated strain and force feedback for high-performance control of piezoelectric actuators," *Sens. Actuators A*, vol. 161, no. 1/2, pp. 256–265, 2010.

[10] Y. Bar-Cohen,, *Electroactive Polymer Actuators as Artificial Muscles: Reality, Potential and Challenges*. Bellingham, WA: SPIE, 2001.

[11] M. Shahinpoor and K. Kim, "Ionic polymer-metal composites: I. Fundamentals," *Smart Mater. Struct.*, vol. 10, pp. 819–833, 2001.

[12] B. Akle, M. Bennett, and D. Leo, "High-strain ionomeric-ionic liquid electroactive actuators," *Sens. Actuators A*, vol. 126, pp. 173–181, 2006.

[13] K. Kim and M. Shahinpoor, "Ionic polymer–metal composites. Part ii. Manufacturing techniques," *Smart Mater. Struct.*, vol. 12, pp. 65–79, 2003.

[14] Z. Chen and X. Tan, "Monolithic fabrication of ionic polymer-metal composite actuators capable of complex deformation," *Sens. Actuators A, Phys.*, vol. 157, pp. 246–257, 2010.

[15] C. Bonomo, L. Fortuna, P. Giannone, S. Graziani, and S. Strazzeri, "A model for ionic polymer metal composites as sensors," *Smart Mater. Struct.*, vol. 15, pp. 749–758, 2006.

[16] Z. Chen, X. Tan, A. Will, and C. Ziel, "A dynamic model for ionic polymer-metal composite sensors,," *Smart Mater. Struct.*, vol. 16, pp. 1477–1488, 2007.

[17] Z. Chen and X. Tan, "A control-oriented and physics-based model for ionic polymer-metal composite actuators," *IEEE/ASME Trans. Mechatronics*, vol. 13, no. 5, pp. 519–529, Oct. 2008.

[18] Z. Chen, D. Hedgepeth, and X. Tan, "A nonlinear, control-oriented model for ionic polymer-metal composite actuators," *Smart Mater. Struct.*, vol. 18, pp. 055008-1–055008-9, 2009.

[19] P. de Gennes, K. Okumura, M. Shahinpoor, and K. Kim, "Mechanoelectric effects in ionic gels," *Europhys. Lett.*, vol. 50, no. 4, pp. 513–518, unskip 2000.

[20] M. Porfiri, "Charge dynamics in ionic polymer metal composites," *J. Appl. Phys.*, vol. 104, no. 10, pp. 104915-1–104915-10, 2008.

[21] A. Abdulsadda and X. Tan, "Underwater source localization using an IPMC-based artificial lateral line," in *Proc. IEEE Int. Conf. Robot. Autom.*, 2011, pp. 2719–2724.

[22] L. Ferrara, M. Shahinpoor, K. Kim, H. Schreyer, A. Keshavarzi, E. Benzel, and J. Lantz, "Use of ionic polymer-metal composites (IPMCS) as a pressure transducer in the human spine," in *Proc. SPIE—Smart Struct. Mater. 1999: Electroactive Polymer Actuators Devices*, 1999, vol. 3669, pp. 394–401.

[23] A. Keshavarzi, M. Shahinpoor, K. Kim, and J. Lantz, "Blood pressure, pulse rate, and rhythm measurement using ionic polymer-metal composite sensors," in *Proc. SPIE—Smart Struct. Mater. 1999: Electroactive Polymer Actuators Devices*, 1999, vol. 3669, pp. 369–376.

[24] T. Ganley, D.L.S. Hung, G. Zhu, and X. Tan, "Modeling and inverse compensation of temperature-dependent ionic polymer-metal composite sensor dynamics," *IEEE/ASME Trans. Mechatronics*, vol. 16, no. 1, pp. 80–89, Feb. 2011.

[25] J. Wang, C. Xu, M. Taya, and Y. Kuga, "Bio-inspired tactile sensor with arrayed structures based on electroactive polymers," in *Proc. SPIE—Electroactive Polymer Actuators Devices*, 2008, vol. 6927, pp. 69271B-1–69271B-8.

[26] P. Brunetto, L. Fortuna, P. Giannone, S. Graziani, and F. Pagano, "A small scale viscometer based on an IPMC actuator and an IPMC sensor," in *Proc. IEEE Instrum. Meas. Technol. Conf.*, 2010, pp. 585–589.

[27] S. D. Peterson, M. Porfiri, and A. Rovardi, "A particle image velocimetry study of vibrating ionic polymer metal composites in aqueous environments," *IEEE/ASME Trans. Mechatronics*, vol. 14, no. 4, pp. 474–483, Aug. 2009.

[28] C. Prince, W. Lin, J. Lin, S. D. Peterson, and M. Porfiri, "Temporally-resolved hydrodynamics in the vicinity of a vibrating ionic polymer-metal composite," *J. Appl. Phys.*, vol. 107, pp. 094908-1–094908-12, 2010.

[29] M. Aureli, V. Kopman, and M. Porfiri, "Free-locomotion of underwater vehicles actuated by ionic polymer metal composites," *IEEE/ASME Trans. Mechatronics*, vol. 15, no. 4, pp. 603–614, Aug. 2010.

[30] Z. Chen, S. Shatara, and X. Tan, "Modeling of biomimetic robotic fish propelled by an ionic polymer-metal composite caudal fin," *IEEE/ASME Trans. Mechatronics*, vol. 15, no. 3, pp. 448–459, Jun. 2010.

[31] W. Yim, J. Lee, and K. J. Kim, "An artificial muscle actuator for biomimetic underwater propulsors," *Bioinspiration Biomimetics*, vol. 2, pp. S31–S41, 2007.

[32] P. Brunetto, L. Fortuna, S. Graziani, and S. Strazzeri, "A model of ionic polymer–metal composite actuators in underwater operations," *Smart Mater. Struct.*, vol. 17, no. 2, pp. 025029-1–025029-12, 2008.

[33] K. Abdelnour, E. Mancia, S. Peterson, and M. Porfiri, "Hydrodynamics of underwater propulsors based on ionic polymer metal composites: A numerical study," *Smart Mater. Struct.*, vol. 18, no. 8, pp. 085006-1–085006-11, 2009.

[34] A. J. MacDaid, K. C. Aw, E. Haemmerle, and S. Q. Xie, "Control of IPMC actuators for microfluidics with adaptive "online" iterative feedback tuning," *IEEE/ASME Trans. Mechatronics*, [Online]. Available: http://ieeexplore.ieee.org, DOI: 10.110.9/TMECH.2011.2135373.

[35] M. Aureli, C. Prince, M. Porfiri, and S. D. Peterson, "Energy harvesting from base excitation of ionic polymer metal composites in fluid environments," *Smart Mater. Struct.*, vol. 19, p. 015003, 2010.

[36] A. Giacomello and M. Porfiri, "Underwater energy harvesting from a heavy flag hosting ionic polymer metal composites," *J. Appl. Phys.*, vol. 109, p. 084903, 2011.

[37] J. Chung and H. Yoo, "Dynamic analysis of a rotating cantilever beam by using the finite element method," *J. Sound Vibrat.*, vol. 249, no. 1, pp. 147–164, 2002.

[38] N. Wereley, G. Wang, and A. Chaudhuri, "Demonstration of uniform cantilevered beam bending vibration using a pair of piezoelectric actuators," *J. Intell. Mater. Syst. Struct.*, vol. 22, no. 4, pp. 307–316, 2011.

[39] A. K. Banerjee and S. Nagarajan, "Efficient simulation of large overall motion of beams undergoing large deflection," *Multibody Syst. Dyn.*, vol. 1, pp. 113–126, 1997.
[40] S. J. Kim, I. T. Lee, and Y. H. Kim, "Performance enhancement of IPMC actuator by plasma surface treatment," *Smart Mater. Struct.*, vol. 16, no. 1, pp. N6–N11, 2007.
[41] W. Thomson and M. Dahleh, *Theory of Vibration With Applications*, 5th ed. Englewood Cliffs, NJ: Prentice-Hall, 1998, pp. 163–187.
[42] P. Heyliger and J. Reddy, "A higher order beam finite element for bending and vibration problems," *J. Sound Vibrat.*, vol. 126, no. 2, pp. 309–326, 1988.
[43] J. Sader, "Frequency response of cantilever beams immersed in viscous fluids with applications to the atomic force microscope," *J. Appl. Phys.*, vol. 84, no. 1, pp. 64–76, 1998.
[44] Z. Chen, Y. Shen, N. Xi, and X. Tan, "Integrated sensing for ionic polymer-metal composite actuators using PVDF thin films," *Smart Struct. Mater.*, vol. 16, pp. S262–S271, 2007.
[45] M. Potter and D. Wiggert, *Mechanics of Fluid*, 2nd ed. Englewood Cliffs, NJ: Prentice-Hall, 1997, pp. 339–343.
[46] J. W. L. Zhou, H.-Y. Chan, T. K.H. To, K. W. C. Lai, and W. J. Li, "Polymer MEMS actuators for underwater micromanipulation," *IEEE/ASME Trans. Mechatronics*, vol. 9, no. 2, pp. 334–342, Jun. 2004.
[47] G.-H. Feng and R.-H. Chen, "Improved cost-effective fabrication of arbitrarily shaped μIPMC transducers," *J. Micromech. Microeng.*, vol. 18, p. 015016, 2008.
[48] G. H. Keulegan and L. H. Carpenter, "Forces on cylinders and plates in an oscillating fluid," *J. Res. Natl Bur. Stand.*, vol. 60, no. 5, pp. 423–440, 1958.
[49] R. A. Bidkar, M. Kimber, A. Raman, A. K. Bajaj, and S. V. Garimella, "Nonlinear aerodynamic damping of sharp-edged flexible beams oscillating at low Keulegan-Carpenter numbers," *J. Fluid Mech.*, vol. 634, pp. 269–289, 2009.

Xuefei Chen received the B.S. degrees in mechanical engineering and electrical engineering from Tianjin University, Tianjin, China, in 2002, where he also received the M.Eng. degree in mechanical engineering in 2005. He is currently working toward the Ph.D. degree in the Department of Mechanical Engineering, Michigan State University, East Lansing.

Between 2005 and 2008, he was with Delphi as a Calibration Engineer of the engine management system. His research interests include modeling and control of automotive engines and hybrid powertrains and biofuel applications for automotive systems.

Mr. Chen is a Student Member of the Society of Automotive Engineers and the American Society of Mechanical Engineers.

Guoming (George) Zhu received the B.S. and M.S. degrees from Beijing University of Aeronautics and Astronautics, Beijing, China, in 1982 and 1984, respectively, and the Ph.D. degree in aerospace engineering from Purdue University, West Lafayette, IN, in 1992.

He is currently an Associate Professor in the Department of Mechanical Engineering and the Department of Electrical and Computer Engineering, Michigan State University, East Lansing. Prior to this, he was a Technical Fellow in advanced powertrain systems with Visteon Corporation. He was also a Technical Advisor at Cummins Engine Co. His teaching interests focus on control classes at both undergraduate and graduate levels. He has more than 24 years of experience related to control theory, engine diagnostics, and combustion control. He has contributed to 100 refereed technical papers and received 40 U.S. patents. His current research interests include closed-loop combustion control of internal combustion engines, engine system modeling and identification, hybrid powertrain control and optimization, linear parameter-varying control with application to automotive systems, etc.

Dr. Zhu was an Associate Editor of the *ASME Journal of Dynamic Systems, Measurement, and Control*, and a member of the Editorial Board of the *International Journal of Powertrain*. He is also a Fellow of the American Society of Mechanical Engineers.

Xiaojian Yang received the B.S. and M.S. degrees in vehicle engineering from Hefei University of Technology, Hefei, China, in 2000 and 2003, respectively, and the Ph.D. degree in mechanical engineering from Michigan State University (MSU), East Lansing, in 2011.

He is currently a Senior Control Engineer in the advanced powertrain group at Delphi Automotive PLC, Troy, MI. Before joining Delphi, he conducted research in modeling and control of homogeneous-charge-compression-ignition engine systems at the Energy and Automotive Research Lab of MSU. His research interests include modeling and control of advanced internal combustion engine systems.

David L. S. Hung received the B.S. degree (with distinction) in mechanical engineering from Iowa State University, Ames, in 1991, and the M.Eng. and Ph.D. degrees in mechanical engineering from Carnegie Mellon University, Pittsburgh, PA, in 1993 and 1998, respectively.

He is currently an Associate Professor of mechanical engineering at the University of Michigan–Shanghai Jiao Tong University Joint Institute, Shanghai, China. He is also a Professor in the School of Mechanical Engineering, Shanghai Jiao Tong University. Previously, he was an Associate Professor in the Department of Mechanical Engineering, Michigan State University, East Lansing. Between 1998 and 2009, he also held positions in the automotive industry at General Motors, Delphi, and Visteon, where he was responsible for developing gasoline direct injection systems and optical diagnostics for in-cylinder fuel mixture preparation and combustion measurements. His research interests include the development and utilization of sustainable energy systems, renewable fuels for vehicle and aviation applications, optical diagnostics, and novel flow sensing techniques.

Dr. Hung is active in various technical organizations such as the Society of Automotive Engineers (SAE), the Institute of Liquid Atomization and Spray Systems, and the Aviation Technical Committee of the Coordinating Research Council. He is leading a task force for the SAE Gasoline Fuel Injection Standards Committee to develop and improve new and existing engineering standards. He has received four SAE International awards, including the 2009 SAE/Interregs Standards and Regulations Award for Young Engineers, for his contributions to developing engineering standards and regulations for the global automotive industry. He is the recipient of the inaugural Shanghai 1000 Scholar Award and also serves on the Editorial Board of *Progress in Energy and Combustion Science*.

Xiaobo Tan (S'97–M'02–SM'11) received the B.Eng. and M.Eng. degrees in automatic control from Tsinghua University, Beijing, China, in 1995 and 1998, respectively, and the Ph.D. degree in electrical and computer engineering from the University of Maryland, College Park, in 2002.

From September 2002 to July 2004, he was a Research Associate with the Institute for Systems Research, University of Maryland. He joined the Faculty of the Department of Electrical and Computer Engineering, Michigan State University (MSU), East Lansing, in 2004, where he is currently an Associate Professor. He is keen to integrate his research with educational and outreach activities, and currently leads a National Science Foundation (NSF)-funded Research Experiences for Teachers Site on Bio-Inspired Technology and Systems at MSU. His current research interests include electroactive polymer sensors and actuators, modeling and control of smart materials, biomimetic robotic fish, mobile sensing in aquatic environments, and collaborative control of autonomous systems.

Dr. Tan is an Associate Editor of *Automatica* and a Technical Editor of the IEEE/ASME TRANSACTIONS ON MECHATRONICS. He served as the Program Chair for the 15th International Conference on Advanced Robotics. He was a Guest Editor of the *IEEE Control Systems Magazine* for its February 2009 issue's Special Section on Modeling and Control of Hysteresis. He received an NSF CAREER Award in 2006, the 2008 ASME DSCD Best Mechatronics Paper Award (with Y. Fang) in 2009, and the Teacher-Scholar Award from MSU in 2010.